Article

Controlling effective field contributions to laser-induced magnetization precession by heterostructure design

Check for updates

Jasmin Jarecki[1,2], Maximilian Mattern [1] ✉, Fried-Conrad Weber[1], Jan-Etienne Pudell[1,3,4], Xi-Guang Wang[5], Juan-Carlos Rojas Sánchez [6], Michel Hehn [6], Alexander von Reppert [1] & Matias Bargheer [1,4] ✉

Nanoscale heterostructure design can control laser-induced heat dissipation and strain propagation, as well as their efficiency for driving magnetization precession. Here, we incorporate MgO layers into the experimental platform of metallic Pt-Cu-Ni heterostructures to block the propagation of hot electrons. We show via ultrafast x-ray diffraction the capability of our platform to control the spatio-temporal shape of the transient heat and strain. Time-resolved magneto-optical Kerr experiments with systematic tuning of the magnetization precession frequency showcase control of the magnetization dynamics in the Ni layer. Our experimental analysis highlights the role of quasi-static strain as a driver of precession when the magnetic material is rapidly heated via electrons. The effective magnetic field change originating from demagnetization partially compensates the change induced by quasi-static strain. The strain pulses can be shaped via the nanoscale heterostructure design to efficiently drive the precession, paving the way for opto-magneto-acoustic devices with low heat energy deposited in the magnetic layer.

Direct optical excitation of ferromagnets triggers phenomena such as ultrafast demagnetization[1–5], coherent magnetization precession[6–18], spin-transport[19–21] and all-optical magnetization switching[22–24]. An optimized excitation of coherent magnetization precession enables precessional switching[25–28]. Most investigations have focused on mechanisms using direct excitation of the magnetically ordered material to drive precession via magnetic anisotropy changes or via magneto-elastic coupling: magneto-crystalline anisotropy is controlled by temperature[6–9], shape anisotropy by demagnetization[6,10,12], and strain effects are distinguished as resulting from quasi-static expansion[11,12] and propagating strain pulses[13–18,27,29].

In a single ferromagnetic layer, the optically deposited energy leads to all at once: ultrafast demagnetization, temperature-induced anisotropy changes, and both quasi-static and propagating strain components, which are all a consequence of the rapid rise of electron-, spin- and phonon-temperatures. Each of these mechanisms can be described as pump-induced changes of effective field contributions that drive coherent magnetization precession, although the effects can cancel each other—calling for handles that turn individual effects on and off. Analysis and control of the induced

precession have been mainly limited to the external magnetic field[6,15], the layer thickness determining the round trip time of acoustic strain pulses[14,18,29], or multipulse excitation schemes tuning the strain pulse pattern[18,30].

Integrating the functional magnetic layer into nanoscale heterostructures adds multiple control scenarios: The heat transport and the propagating picosecond strain pulses can be tuned individually by transparent capping layers[31,32], metal–insulator superlattices[33,34] and functional transducers with tunable stress generation mechanisms via temperature and fluence[35–37] or magnetic fields[38]. In addition, the combination of metals with different electron–phonon coupling strengths and insulating interlayers modify the heat transport within the heterostructure[39–45], which enables the control of both the launched propagating strain pulses and the excitation of the functional magnetic layer.

Recently, metallic heterostructures built of an optically excited transducer, a propagation layer with weak electron-phonon coupling, and a buried functional magnetic layer have become intensively investigated[19,20,43–51]. Laser-excited hot electrons traveling through the

[1]Institut für Physik & Astronomie, Universität Potsdam, 14476 Potsdam, Germany. [2]Max-Born-Institut für Nichtlineare Optik und Kurzzeitspektroskopie, 12489 Berlin, Germany. [3]European X-Ray Free-Electron Laser Facility, Schenefeld, Germany. [4]Helmholtz-Zentrum Berlin für Materialien und Energie, BESSY II, 12489 Berlin, Germany. [5]School of Physics and Electronics, Central South University, Changsha 410083, China. [6]Institut Jean Lamour (UMR CNRS 7198), Université Lorraine, 54000 Nancy, France. ✉e-mail: mamattern@uni-potsdam.de; bargheer@uni-potsdam.de

propagation layer induce ultrafast demagnetization in buried metallic magnetic layers[44,45,50,51], drive magnetization switching[20,49] and excite precession[46] and higher order standing spin waves in buried dielectric ferromagnetic layers[47,48]. Previous experiments have reported a controllable attenuation and elongation of this hot electron pulse via additional metallic interlayers exhibiting strong electron-phonon coupling[44,45]. However, a thorough and simultaneous experimental assessment of the strain, heat, and magnetization dynamics in such functional heterostructures is lacking.

Here, we tailor the rapid distribution of the optically deposited energy within a Pt–Cu–Ni heterostructure by inserting an insulating MgO interlayer that stops the heat transport via electrons. We quantify the resulting strain response of the metallic layers via ultrafast X-ray diffraction (UXRD), to deduce the tailored heat transport and the shape of the strain pulses. The transient response of the buried functional Ni layer strongly depends on the position of the MgO interlayer, either before or after the Cu layer. Utilizing the polar time-resolved magneto-optical Kerr effect (trMOKE), we probe the laser-induced change of the out-of-plane magnetization and identify the mechanisms (demagnetization, quasi-static strain, and propagating strain), which drive coherent precession as a function of the angle of the external magnetic field provided by a rotatable permanent magnet. We observe a pronounced dependence of the angle-dependent precession amplitude on the heterostructure design. We model the different responses of the heterostructures with a unique set of parameters by inputting the transient strain and heat—quantified by UXRD—into the Landau–Lifshitz Gilbert (LLG) equation. We discuss the concepts of how heterostructure design can control magnetization precession: The thickness of the propagation layer—and hence the total multilayer stack—sets the round trip time, which can be made resonant with the precession frequency that is tuned via the external magnetic field angle. The position of the MgO interlayer controls the thickness of the metal transducer and hence tailors the shape of the strain pulses, which are most efficient in driving the magnetization precession by matching the timing of both expansive and compressive strain to the phase of the precession. Generally, the MgO interlayer—or alternatively any other insulating material—disables the ultrafast demagnetization and quasi-static expansion of the Ni layer as driving mechanisms that otherwise drive precession efficiently for out-of-plane external fields.

Our report on the combined study of trMOKE and UXRD experiments is structured as follows: We first present the magnetization dynamics triggered in three Pt–Cu–Ni heterostructures that only differ in the position of an insulating MgO layer. The next subsection shows how UXRD quantifies the transient strain and heat in these heterostructures before the modeling subsection discusses a solution of the LLG equation, where the extracted strain profile is used as an input parameter for the transient effective magnetic field.

Results and discussion
Observation of the magnetization precession by trMOKE
In the all-optical trMOKE experiment sketched in Fig. 1a, the three heterostructures shown in Fig. 1b are excited by a near-infrared laser pulse with a pump energy density of 7.5 mJ cm^{-2}. The femtosecond pump pulse is mainly absorbed by the 7–10 nm thick Pt cap layer[43]. While all heterostructures share the same structure of a Pt cap, a thick Cu transport, and a 22 nm buried Ni layer, they mainly differ by the ultrafast energy transfer between the Pt and Ni layer that is supported by the electrons in the Cu layer in sample 1 but suppressed by an insulating MgO interlayer either below or in front of the Cu layer in samples 2 and 3, respectively.

Figure 1c shows the polar trMOKE signal, i.e., the transient change of the out-of-plane magnetization ΔM_z in $\Delta \xi = 5°$ steps for a full rotation of the magnet for sample 1. The variation from out-of-plane (0° and 180°) to in-plane (90° and 270°) external magnetic fields shows a fourfold symmetry of the precession. Therefore, we only discuss the range from 0 to 90° in the following. The Fourier transform of these data in Fig. 1d reveals an increasing precession frequency as the out-of-plane component of the external field decreases and the magnetization tilts towards the sample plane, which represents the magnetic easy axis. Since the external magnetic

field $\mu_0 H_{ext} = 390$ mT is below the saturation field $\mu_0 H_{sat} = 620$ mT, the magnetization is always oriented along an angle between the external field and the sample plane before laser excitation. Figure 1e, f shows the same dependence of the precession frequency on the rotation angle ξ for samples 2 and 3. The color code for the precession amplitude shows that the presence of the MgO layer in these samples suppresses the excitation of precession for an out-of-plane orientation of the external field ($\xi = 0°$), which is pronounced for the purely metallic sample 1. All three samples, however, exhibit a maximum amplitude around $\xi = 47°$, with a considerably smaller amplitude for sample 3.

Figure 2 directly compares the driven magnetization precession in the three magnetic heterostructures: The extracted frequency in panel b confirms that the angle-dependence of the precession frequency is the same for all three Ni layers. Panel a provides a comparison of the precession amplitudes extracted from the fast-Fourier-transform (FFT). Indeed all samples show a maximum at the external magnetic field angle $\xi = 47°$ for which the precession frequency matches the inverse round-trip time $T = L/v_s$ of longitudinal strain pulses through the multilayer stack (dashed horizontal line), which is essentially given by the total thickness L and the thickness-weighted average sound velocity v_s. While in the presence of a MgO interlayer (samples 2 and 3) the precession amplitude rapidly decreases for larger and smaller ξ values until it completely vanishes, we observe an additional increase of the precession amplitude towards $\xi = 0°$ in the absence of a MgO interlayer. These systematics already hint at the fact that the maximum at intermediate angles is a magneto-acoustic resonance that links the precession to the propagating strain pulses. In contrast, the low-frequency precession close to $\xi = 0°$ is only enabled by the rapid heat transfer into Ni via hot electrons that leads to ultrafast demagnetization and an expansion.

The time-domain out-of-plane magnetization responses (symbols) shown in Fig. 2c, d provide further insights into the laser-induced driving of the magnetization precession. In the absence of a MgO interlayer, we clearly observe an ultrafast demagnetization originating from the rapid excitation of the Ni layer by hot electrons. This rapid excitation drives a precession at $\xi = 5°$, which is absent in samples 2 and 3, where electrons are stopped by the MgO interlayer, and we only observe a slow demagnetization within hundreds of picoseconds (yellow and blue transients in Fig. 2). At $\xi = 47°$ we observe pronounced oscillations of varying amplitude for all three heterostructures. The precession amplitude even slightly increases from the first to the second maximum, indicating the periodically acting driving force by propagating strain pulses. In addition, we note an immediate start of the precession upon laser-excitation in samples 1 and 2, while sample 3 clearly responds not earlier than at about 20 ps, which is the time it takes acoustic strain pulse to travel from the excited Pt cap layer through the Cu layer.

Similar qualitative assignments rationalizing the origin of precession are common in the literature. In the following, we quantify the laser-induced strain response of the Ni layer and its transient temperature increase by UXRD. Using the measured transient temperature rise and the laser-induced strain as input for our LLG model described in the modeling section nicely captures the heterostructure-dependent precession (solid lines in Fig. 2) and unambiguously identifies the role of the different driving mechanisms.

Characterization of strain and heat via UXRD
In the UXRD experiment, the Pt–Cu–Ni heterostructures are excited by femtosecond p-polarized laser pulses with a central wavelength of 800 nm, as in the trMOKE experiment. We probe the transient layer-specific expansion by the shift of the layer-specific Bragg peaks with the reciprocal space slicing method[52] at a laser-driven table-top plasma X-ray source[53].

Figure 3 displays a schematic of the UXRD setup and the measured (111) Bragg peaks of the Pt, Cu, and Ni layers of sample 1. Their positions along the reciprocal space coordinate q_z encode the average out-of-plane lattice constants d of the respective layer via $q_z = 2\pi/d$. The shift of the separated Bragg peaks along q_z yields the layer-specific transient strain $\eta = \Delta d/d_0$ as a relative change of the average out-of-plane lattice constant Δd

Fig. 1 | Magnetization precession depends on the orientation of the external magnetic field. a Sketch of the transient magneto-optical Kerr effect (trMOKE) experiment, including a rotatable permanent magnet that provides a magnetic field of $\mu_0 H_{ext} = 390$ mT at an angle ξ with respect to the sample normal. **b** Schematics of the three heterostructures with the Pt cap layer as the main light absorber and Cu as the propagation layer for hot electrons. Sample 1 is a purely metallic structure, and samples 2 and 3 contain a MgO layer to stop electron propagation. **c** Polar trMOKE measured for sample 1 for a full rotation of the external magnetic field by 360°. The oscillating out-of-plane magnetization change $\Delta M_z(t)$ is color-coded (red positive and blue negative). See Fig. 2c, d for cuts at a certain magnetic field angle ξ. **d** Fast Fourier transformation (FFT) of the trMOKE signal shows an increase of the precession frequency with in-plane orientation of the external field and a maximum FFT amplitude A for 0° and 47°. **e, f** Same for samples 2 and 3, where only the maximum at 47° is observed.
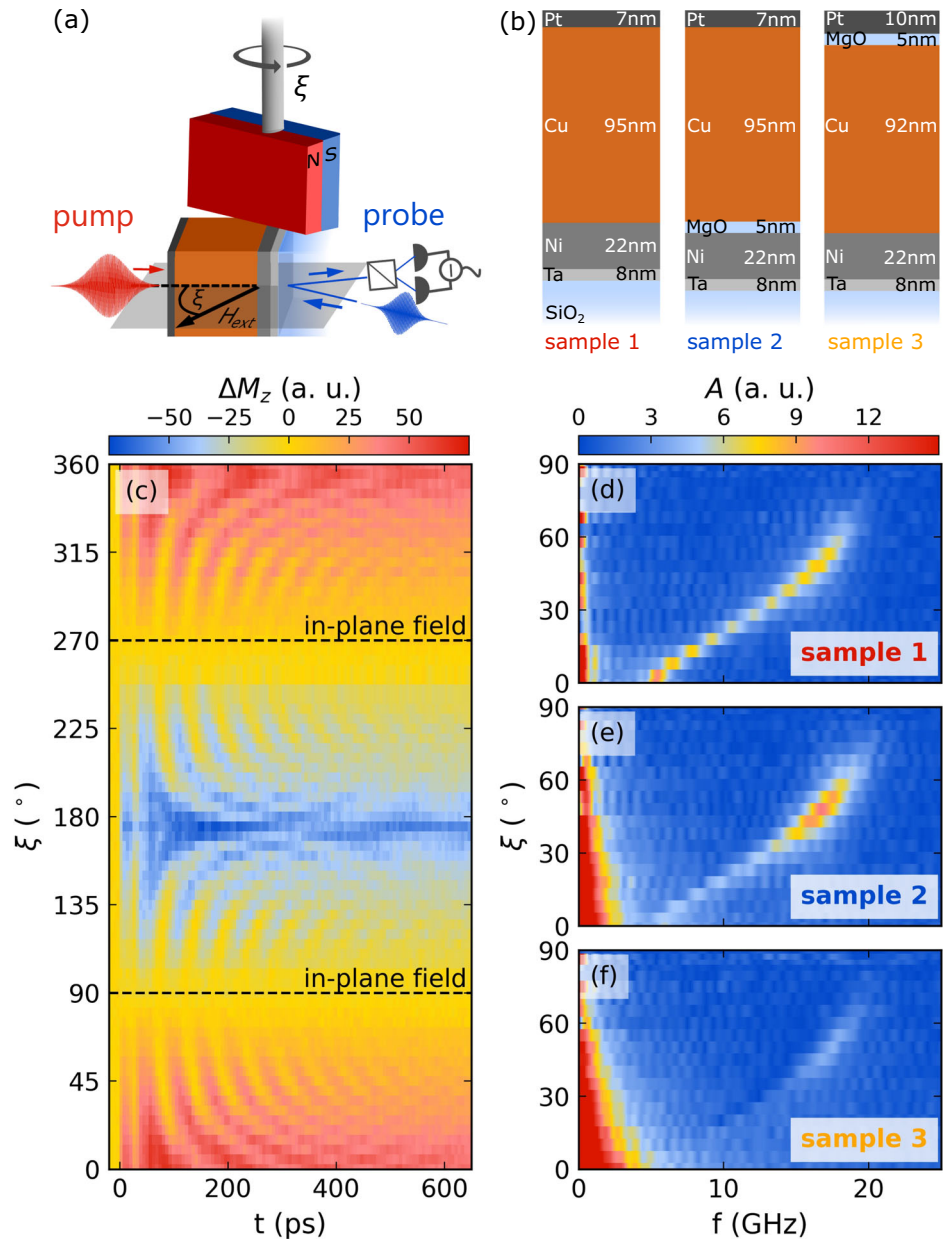

with respect to its value d_0 before excitation. Figure 3c–e displays the measured layer-specific strain responses (symbols) to excitation of 13.2 mJ cm^{-2} for samples 1 and 2 and 7.5 mJ cm^{-2} for sample 3 chosen to avoid damage to the MgO interlayer. The solid lines represent the modeled transient strain response of the heterostructures utilizing the modular PYTHON library UDKM1DSIM[54] and a single set of thermo-physical parameters stated in Table 1 in the methods section.

In all three heterostructures, the optically deposited energy to the Pt layer induces an expansion that peaks at 1.5 ps (Fig. 3c) when the expansive strain pulses launched at the surface and the Pt–Cu interface have propagated through the Pt layer at the speed of sound $v_{Pt} = 4.2$ nm ps^{-1}[55]. The following strain oscillation can be interpreted as a breathing of the Pt layer with a $T_{Pt} = 2L_{Pt}/v_{Pt} \approx 3$ ps period determined by the layer thickness L_{Pt}. The partial transmission of strain pulses through the impedance mismatched Pt–Cu or Pt–MgO interfaces leads to a decay of the oscillation of the Pt layer thickness within tens of picoseconds. This propagating strain pulse is superimposed on the quasi-static expansion of Pt due to heating. While the oscillatory Pt response is very similar for all three heterostructures, the quasi-static expansion is much increased for sample 3, where the MgO layer

keeps the thermal energy within Pt because it prohibits electronic heat transport from Pt into the thick Cu film.

This suppression of the rapid excitation of Cu as well as the buried Ni layer in sample 3, results in a delayed expansion within hundreds of picoseconds due to slow energy transfer into these layers via phonons. Therefore, the strain response within the first tens of picoseconds is dominated by the strain pulse with leading compression driven by the rapid expansion of the Pt layer. This strain pulse immediately compresses the adjacent Cu layer and subsequently also compresses the Ni layer when it enters at 20 ps after having propagated through Cu. In sample 2, moving the MgO interlayer in front of Ni enables rapid distribution of the optically deposited energy among Pt and Cu via hot electrons[43]. This rapid excitation of Cu results in a rapid expansion (Fig. 3d) that shortens the initial compression by the expanding Pt layer. The expansion of Cu drives a bipolar strain pulse that compresses the buried Ni layer immediately within the first picoseconds—not waiting for strain propagation from the surface - and superimposes with the strain pulse launched by Pt entering Ni at 20 ps. The strong oscillation of the average strain of Cu with the period matching twice the transit time through the entire heterostructure

Fig. 2 | Heterostructure-dependent magnetization precession. a Precession amplitude A as a function of the orientation of the external magnetic field. The extracted experimental data (symbols) are well reproduced via the Landau–Lifshitz–Gilbert (LLG) model described in the modeling section (solid lines) for all three heterostructures. All samples show a resonant enhancement at an angle where the precession frequency (panel b) matches the inverse round-trip time of the propagating strain pulses, highlighted in Fig. 3e) as black arrows. The black solid line denotes the hypothetical precession amplitude for sample 1 without any contribution from propagating strain pulses. **b** Measured precession frequency f (symbols) that is independent of the heterostructure since all structures share the same Ni layer. **c, d** Laser-induced change of the out-of-plane magnetization ΔM_z that displays the heterostructure-dependent demagnetization and magnetization precession at $\xi = 5°$ and $\xi = 47°$, respectively. The solid colored lines represent our LLG model, while the gray solid lines represent the magnetization precession if we neglect the ultrafast demagnetization as a driver of the precession in sample 1. The results are offset for clarity.
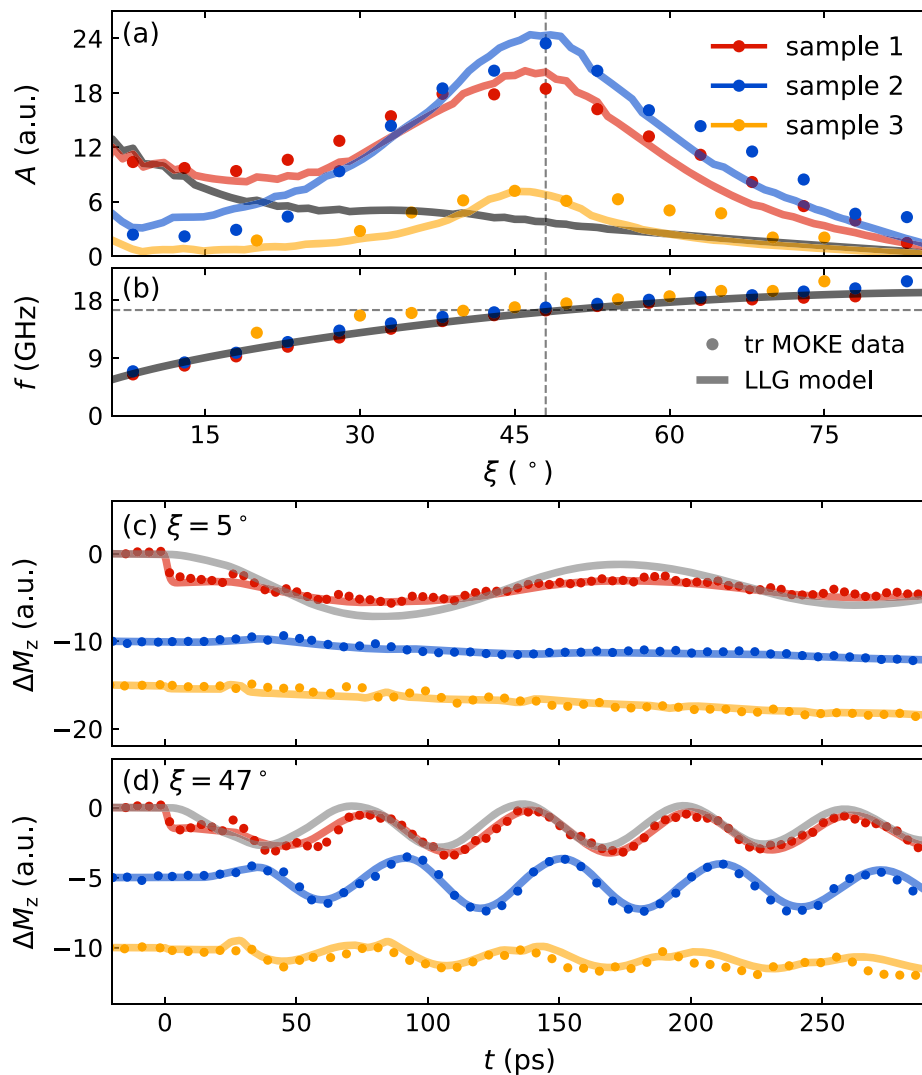
is strongly suppressed in sample 1, where the MgO layer prevents energy transport to Cu via electrons.

Removing the MgO interlayer enables an additional fast diffusive transport of hot electrons from the optically excited Pt layer to the buried Ni through Cu, as observed previously[43]. Equilibration of the electronic system is very fast, and the large electronic heat capacity and the strong electron-phonon coupling in Ni originating from the large density of states of flat 3d-bands close to the Fermi level rapidly localizes a large fraction of the deposited energy in Ni. For our heterostructures with a 100 nm thick Cu layer, details such as initial ballistic or superdiffusive transport are not relevant, as we merely differentiate sub-picosecond heat transport by electrons from slower transport via phonons. The large amount of energy deposited to Ni drives an expansion that launches an additional compression into the adjacent Cu layer extending its compression to 6 ps. In total, the strain response of Ni is the superposition of its quasi-static expansion due to heating and the strain pulses launched by Cu, Pt, and Ni. The strain pulse emerging from Pt enters Ni at 20 ps and is reflected at the substrate and the surface several times, as indicated by the arrows in Fig. 3e.

Our model of the layer-specific transient strain response (solid lines) reproduces these experimental observations for all three layers in all three heterostructures with a single parameter set. The model therefore yields the transient average electron $T_{\mathrm{Ni}}^{\mathrm{el}}(t)$ and phonon $T_{\mathrm{Ni}}^{\mathrm{ph}}(t)$ temperature as well as the average transient strain $\eta_{\mathrm{Ni}(t)}$ of the buried Ni layer in all three heterostructures. In the following, these quantities

validated by the good agreement of our model with the UXRD experiment serve as input for our LLG model of the heterostructure-dependent magnetization precession.

Modeling of the magnetization precession and discussion

In this section, we relate the heterostructure-dependent strain response and heating of the Ni layer quantified by UXRD in the previous section to the precession observed by polar trMOKE and discuss how heterostructure design can control the driving mechanisms of magnetization precession.

We model the precessional motion of the macrospin vector $\mathbf{M}(t) = M_{\mathrm{sat}}(m_x(t)\mathbf{e}_x + m_y(t)\mathbf{e}_y + m_z(t)\mathbf{e}_z)$ that represents the average magnetization of the Ni layer in the heterostructures utilizing the LLG equation:

$$\frac{\partial \mathbf{m}}{\partial t} = -\gamma \mu_0 \mathbf{m} \times \mathbf{H}_{\mathrm{eff}} + \alpha \mathbf{m} \times \frac{\partial \mathbf{m}}{\partial t}, \qquad (1)$$

where γ represents the gyromagnetic ratio and α the phenomenological Gilbert damping. The effective field $\mathbf{H}_{\mathrm{eff}}(t)$ drives the magnetization precession and is determined by the material-specific free energy of the macroscopic magnetization F_{M} via $\mu_0 \mathbf{H}_{\mathrm{eff}} = -\nabla_{\mathbf{M}} F_{\mathrm{M}}$. In our model of the macrospin in Ni, we consider a Zeeman energy originating from the external magnetic field $\mathbf{H}_{\mathrm{ext}}$, a shape anisotropy resulting from the thin film geometry and a magneto-acoustic contribution induced by the

Fig. 3 | Ultrafast X-ray diffraction (UXRD) quantifies heat transport and layer-specific strain. **a** Sketch of the UXRD geometry: The detector records layer-specific Bragg peaks separated along the reciprocal space coordinate q_z. **b** Integration of the detector signal along q_y yields a reciprocal space slice, which encodes the mean out-of-plane lattice constant of the Pt, Cu, and Ni layers within the heterostructures. **c** Laser-induced strain response of the Pt layer (symbols) determined from the transient shift of the Bragg peak. The excitation fluence of 13.2 mJ cm^{-2} for samples 1 and 2 was reduced to 7.5 mJ cm^{-2} for sample 3 to avoid damage to the MgO interlayer. The strain responses of the Pt capping layer are offset for clarity. The solid lines represent our model of the transient strain response utilizing the modular PYTHON library UDKM1DSIM[54] and a single set of thermo-elastic parameters collected in Table 1. Introducing a Pt/MgO interface considerably slows down the cooling of Pt, and the increased impedance mismatch enhances the initial fast oscillations. **d**, **e** Laser-induced strain response for the Cu and Ni layers. Note the clear difference of the initial response of the Ni layer, which is expansive for sample 1, compressive for sample 2, and zero for sample 3. The black arrows indicate the arrival of the large amplitude strain pulse launched by the rapid Pt expansion. This periodicity of the Ni strain drives the magnetic resonance shown in Fig. 2a). The transient strain responses of samples 1 and 2 are reproduced from our previous publication[42].
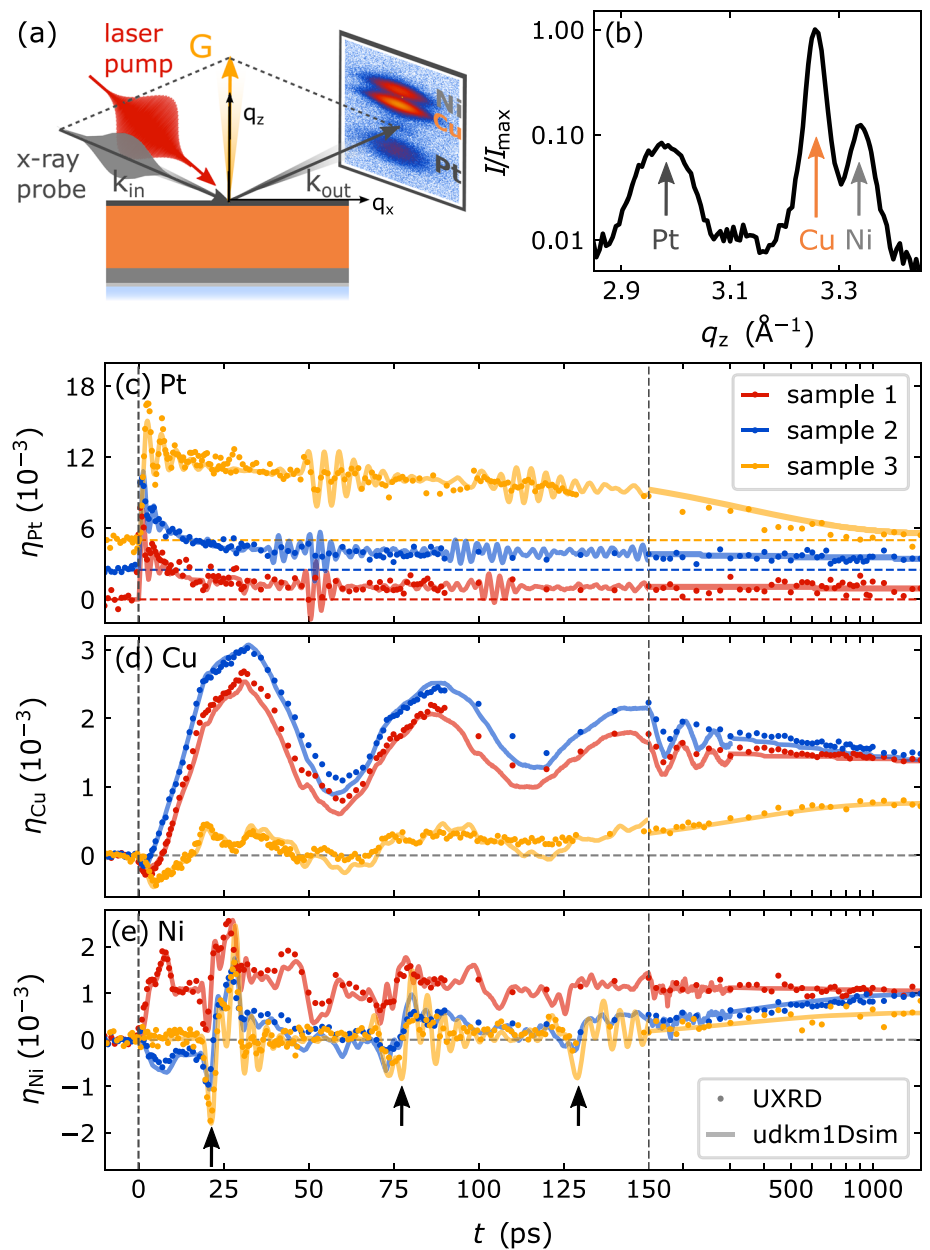

Table 1 | Literature values for the physical parameters of the strain model

	Pt	Cu	Ni	Ta	MgO	glass
$\bar{n}$	$0.576 + 8.078i$[58]	$0.105 + 5.141i$[58]	$2.322 + 8.882i$[58]	$0.992 + 7.293i$[58]	1.728[59]	1.5[60]
γ^S (mJ cm^{-3} K^{-2})	0.73[61]	0.10[62]	1.06[61]	0.38[63]	–	–
C_{ph} (J cm^{-3} K^{-1})	2.85[64]	3.44	3.94[65]	2.33[63]	3.32[66]	1.80[60]
κ^0_{el} (W m^{-1} K^{-1})	66[67]	396[61]	81.4[61]	52.0	–	–
κ_{ph} (W m^{-1} K^{-1})	5.0[67]	5.0	9.6[61]	5.0	50[68](2.5)	1.0[60]
g (PW m^{-3} K^{-1})	375[69]	95[62]	360[62]	100	–	–
ρ (g cm^{-3})	21.45	8.96	8.91	16.68	3.58	2.54[60]
v_S (nm ps^{-1})	4.2[55]	5.2[70]	6.3[71]	4.2[72]	9.1[73]	5.7[60]
Γ_{el}	2.4[74](1.2)	0.9[74]	1.4[75]	1.3[74]	–	–
Γ_{ph}	2.6[76]	2.0[77]	1.8[75]	1.6[74]	1.7[78]	0.3[60]

The complex refractive index $\tilde{n}$, the Sommerfeld constant γ^S, the specific heat of the phonons C_{ph}, the electron-phonon coupling constant g, and the electron κ^0_e and phonon κ_{ph} heat conductivity determine the spatio-temporal energy distribution upon laser-excitation in the framework of a diffusive two-temperature model[42,43]. The subsystem-specific Grüneisen parameters Γ_{el} and Γ_{ph} linearly relate the spatiotemporal energy density to elastic stress on the lattice driving a quasi-static expansion and strain pulses propagating with sound velocity v_S according to the elastic wave equation[42]. Values in brackets are optimized values for the strain modeling. The significant reduction of the thermal conductivity of the MgO interlayer is related to a Kapitza interface resistance.
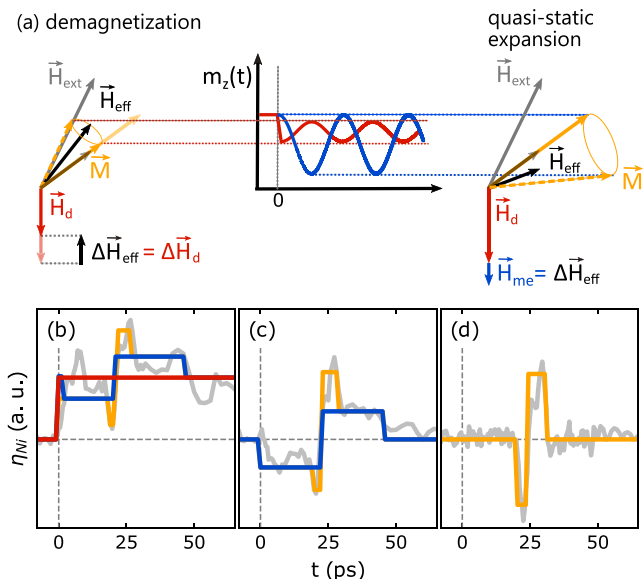
Fig. 4 | Driving mechanisms of the precession. a Sketch of the change of the effective field induced by demagnetization and quasi-static expansion. The dotted lines indicate the maximal excursions of the magnetization vector. The demagnetization yields a very rapid decrease of the z-component of the magnetization m_z, and a concomitant change of the effective magnetic field $\Delta\mathbf{H}_\text{eff}$, whereas the quasi-static expansion only induces a $\Delta\mathbf{H}_\text{eff}$ with opposite sign according to Eq. (2). The black and dark-gray arrows indicate $\mathbf{H}_\text{eff}$ after and before switching on the demagnetization and quasistatic expansion, respectively. Note that strain pulses, i.e., time-dependent strain $\eta(t)$, yield similar time-dependent changes of the effective field with both polarities. **b** The measured transient strain of the Ni layer in sample 1 is separated into a strong step-like quasi-static expansion (red), a long bipolar strain pulse launched by the thick Cu layer (blue), and a sharper strain pulse originating from Pt (yellow). **c** Same for sample 2, where the quasi-static expansion is missing because MgO prevents energy flow into Ni. **d** Same for sample 3, where only the strain pulse from Pt persists, as the MgO layer confines the energy there.

average out-of-plane strain within the Ni layer $\eta_\text{Ni}(t)$:

$$
\begin{aligned}
\mathbf{H}_\text{eff}(\mathbf{m}, \eta) &= \mathbf{H}_\text{ext} - \mathbf{H}_\text{d} - \mathbf{H}_\text{me} \\
&= \mathbf{H}_\text{ext} - M_\text{sat}m_z(t)\mathbf{e}_z - \frac{2b_1\eta_\text{Ni}(t)}{\mu_0 M_\text{sat}}m_z(t)\mathbf{e}_z.
\end{aligned} \quad (2)
$$

In agreement with previous studies in Ni[11,12], we neglect any magneto-crystalline anisotropy, which is supported by a negligible in-plane saturation field for all samples and a quantitative agreement of the out-of-plane saturation field of 620 mT with $\mathbf{H}_\text{d}$ for the measured saturation magnetization M_sat (see Methods section for details). The parameter b_1 determines the strength of the coupling of the laser-induced strain to the out-of-plane magnetization M_z. In addition to the magneto-elastic coupling, our model considers the demagnetization of Ni as the driving mechanism of magnetization precession. The reduced length of the magnetization vector $\mathbf{m}(T_\text{Ni}^\text{ph}(t))$ as function of the phonon temperature T_Ni^ph introduces a change of the effective field via the changing demagnetization field. Here we assume the static reduction of the magnetization $M(T)$ according to VSM measurements. We numerically tested that a very short-lived demagnetization that could be expected for ultrafast laser excitation would not change the slow precessional dynamics considerably. The transient strain $\eta_\text{Ni}(t)$ and the transient temperature $T_\text{Ni}^\text{ph}(t)$ of the Ni layer are not adjustable parameters in our model: We use the time dependence that is quantified from modeling the laser-induced strain response of all three layers in the UXRD experiment. For all three heterostructures, we use the same set of parameters. The methods section collects the measured magnetic properties of the 20 nm Ni film, which are essentially identical in all three heterostructures. From the UXRD experiment, we have calibrated the

spatio-temporal temperature $T(z, t)$ profile and, in particular, the average transient strain $\eta_\text{Ni}(t)$ of the Ni layer. When fitting the measured precession amplitude, this procedure calibrates the magneto-acoustic coupling parameter $b_1 = -8.2 \times 10^6$ J m^{-3}, in rough agreement with previous studies on polycrystalline Ni[12,29].

With an excellent match to the experimental data, Fig. 2a, b displays the modeled precession frequency and amplitude for all heterostructures as a function of the angle ξ of the external magnetic field. According to Eq. (2), the precession frequency increases with ξ due to an increasing H_eff as the demagnetization field $\mathbf{H}_\text{d}$ only compensates the out-of-plane component of the external field while its in-plane component prevails. A comparison of the model to the time-domain out-of-plane magnetization response in Fig. 2c, d also confirms an excellent match regarding the phase of the precession and the temperature-induced demagnetization.

Based on our model of the effective field $\mathbf{H}_\text{eff}$ in Eq. (2), we distinguish two main contributions to the laser-induced change of the effective field: (i) the demagnetization of Ni originating from the laser-induced temperature increase in Ni and (ii) the transient strain in Ni that is the superposition of a quasi-static expansion and propagating strain pulses. In the absence of a MgO interlayer, the rapid heating of Ni induces both demagnetization and quasi-static expansion. Figure 4a illustrates their counteracting influence on the effective field in Ni. The ultrafast demagnetization shortens the magnetization vector $\mathbf{m}$. This reduces the demagnetization field $\mathbf{H}_\text{d}$ via the reduced out-of-plane component m_z. As a result, the effective field change $\Delta\mathbf{H}_\text{eff} = \Delta\mathbf{H}_\text{d}$ points along the positive z-direction, and the shorter magnetization vector precesses around the new effective field $\mathbf{H}_{\text{eff},0} + \Delta\mathbf{H}_\text{eff}$. In contrast, the magneto-elastic field $\mathbf{H}_\text{me}$ induced by the expansion of Ni causes an additional contribution to the effective field pointing along the negative z-direction. This opposite change of the effective field results in opposite starting directions of the precession, corresponding to a phase shift of π. If we neglect the demagnetization as a driving mechanism, the agreement of the model (gray solid line) with the experimentally observed precession in Fig. 2c, d is much worse. Especially, the precession amplitude at $\xi = 5°$ (Fig. 2c) is much larger without demagnetization, which counteracts the effective field due to quasi-static strain. The fact that the precession for sample 1 and $\xi = 5°$ starts with an additional decrease of m_z after the demagnetization indicates the dominance of the quasi-static strain over the demagnetization contribution. At $\xi = 47°$ (Fig. 2d), the model neglecting demagnetization leads to a severe phase shift. In Fig. 2a, the black solid line represents the modeled precession amplitude considering only the quasi-static expansion and demagnetization of Ni in sample 1. The maximum around $\xi = 47°$ is absent without propagating strain pulses, which provide a driving force of the magnetization precession that is resonant with the precession frequency at this angle.

To rationalize the characteristic dependence of the precession amplitude on the heterostructure design, we reconsider the transient strain response of Ni $\eta_\text{Ni}(t) = \eta_\text{qs}(t) + \eta_\text{P}(t)$ quantified by UXRD that is the superposition of a quasi-static strain η_qs and propagating strain pulses η_P launched by rapidly expanding layers. Figure 4b–d dissects the heterostructure-dependent $\eta_\text{Ni}(t)$ into contributions highlighted in different colors. While for sample 3 (panel d), only a sharp bipolar strain pulse launched by the expansion of the Pt layer is present, sample 2 (panel c) exhibits a superposition of this strain pulse from Pt and a pulse with a longer period that is attributed to the expansion of the thicker Cu layer. For the all-metallic sample 1 (panel b), the ultrafast energy transfer to the Ni layer additionally yields its quasi-static expansion highlighted in red.

The UXRD of the Ni layer (Fig. 3e) evidences a periodic contribution to the strain $\eta_\text{Ni}(t)$ in Ni, highlighted by the arrows. The period is given by the round-trip time at the speed of sound through the metallic heterostructure of 57 ps from the Ta–glass interface to the surface and back. This periodic driving force most efficiently drives the magnetization precession when it matches the precession frequency, which results in a maximum precession amplitude at $\xi = 47°$ and $f = 17.5$ GHz for all three heterostructures. In an alternative picture, this maximum precession amplitude relates to
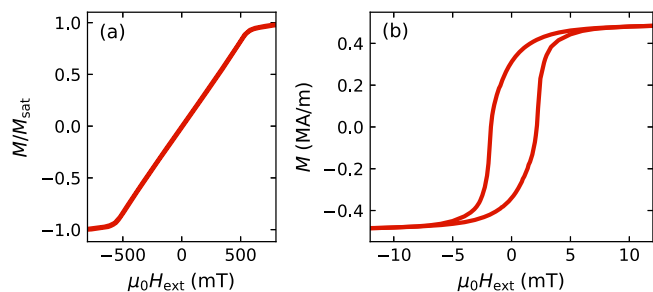
Fig. 5 | Magnetic characterization of the Ni layer. a Out-of-plane hysteresis of (sample 1) measured by polar magneto-optical Kerr effect (MOKE) which accesses the relative magnetization M/M_{sat} and (**b**) in-plane hysteresis measured by vibrating sample magnetometry (VSM) using a (superconducting quantum interference device) SQUID to determine the saturation magnetization M_{sat}.

considerable Fourier amplitude at the precession frequency from the repetition of the bipolar pulses with the same round trip time of about 57 ps through the entire heterostructure[25,29]. However, the efficiency of this magneto-acoustic resonance depends on the shape of the strain pulse. The reduced precession amplitude for sample 3 in comparison to sample 2 highlights that despite its large amplitude, the spatially narrow high-frequency strain pulse launched by the Pt layer drives the magnetization precession less efficiently than the spatially extended strain pulse with low amplitude, which is launched by the Cu layer. We attribute this to the fact that the ≈ 40 ps period of the Cu strain pulse efficiently matches the phase of the positive and negative excursions of the strain pulse to the phase of the magnetization precession. In contrast, within a small fraction of the precession period, the large effects of the positive and negative strain in the bipolar pulse launched by the Pt layer nearly cancel.

Conclusion

In summary, we conducted systematic UXRD and trMOKE experiments on a series of nanoscale metallic heterostructures with a buried functional magnetic layer in order to achieve consistent modeling of the magnetization dynamics based on the measured transient strain and temperature. The excellent agreement for varying heterostructure design and external magnetic field confirms the predictive power of the modeling. Here, we identified the mechanisms driving magnetization precession in Ni and demonstrated their control by tailoring the heat transport within Pt–Cu–Ni heterostructures via insulating MgO interlayers.

The insulating MgO interlayer stops the heat transport via electrons, which disables the quasi-static expansion and ultrafast demagnetization as driving mechanisms by suppressing the rapid excitation of the buried Ni layer. In the absence of a MgO interlayer, the expansion, and demagnetization provide counteracting mechanisms that drive the precession most efficiently for out-of-plane magnetic field orientations. The precession phase reveals the quasi-static expansion as the dominant driver in the explored fluence regime. This efficient magneto-acoustic mechanism is similarly active at an external field orientation that brings the precession into resonance with acoustic sound propagation through the multilayer stack. By considering the actual shape of the strain pulses quantified by UXRD, we moreover show that in addition to this resonance, magneto-acoustic efficiency is boosted roughly by a factor 3 by phase matching, i.e., when positive and negative strain contributions each act on the magnetization vector for about half of the precession period.

Our experiment demonstrates the crucial role of laser-induced strain as a driving mechanism of magnetization precession and highlights heterostructure design as a promising approach to tune the efficiency of driving the magnetization precession that is central to paving the way towards coherent magnetization switching via strain. In this publication, the heterostructure

serving as an effective tuneable transducer consists of simple metals and an insulating layer blocking the heat transport via electrons. In future applications, the controlled manipulation of buried layers by heterostructures can be extended. Multi-pulse coherent-control scenarios can exploit the counteracting influence of demagnetization and strain[56]. A broader range of functional heterostructures can profit from our analysis when choosing materials with stress generation mechanisms or heat transport properties that can be tuned by external parameters such as temperature or electric and magnetic fields.

Methods

Sample growth and characterization

The metal heterostructures (Fig. 1b) consisting of a 7–10 nm thick Pt cap layer, a 95 nm-thick Cu transport layer, and a buried 22 nm Ni layer were sputtered onto glass substrates (Corning 1737 AMLCD). The 8 nm amorphous Ta seed layer ensures textured crystalline growth of Ni, Cu, and Pt with (111)-orientation.

As an input of the modeling of the magnetization precession, we characterized the magnetic properties of the Ni layers. Figure 5 displays the out-of-plane and in-plane hysteresis of sample 1 that are nearly identical to the other samples. We found a saturation magnetization of $M_{sat} = 4.9 \times 10^5$ A m^{-1} via vibrating sample magnetometry (see Fig. 5b). The shape anisotropy parametrized by the demagnetization field $\mu_0|\mathbf{H}|_d = \mu_0 M_s m_z = 620$ mT matches the out-of-plane saturation field determined by polar MOKE (see Fig. 5a). The in-plane hysteresis in Fig. 5b indicate a negligible in-plane anisotropy. In addition, we performed ferromagnetic resonance (FMR) measurements on a very similarly grown Ni film without the Pt–Cu heterostructure determining the gyromagnetic ratio $\gamma/2\pi = 30.8$ GHz T^{-1}.

MOKE measurement

In the all-optical trMOKE experiment sketched in Fig. 1a, the Pt–Cu–Ni heterostructures are excited from the Pt side by a 100 fs pump-pulse with a central wavelength of 800 nm at normal incidence with a repetition rate of 0.5 kHz, a beam footprint of 580×480 μm^2 and a pump energy density of 7.5 mJ cm^{-2}. We probe the transient out-of-plane magnetization of the Ni film through the glass substrate by detecting the polarization rotation of a reflected 400 nm probe pulse. A commercial rotatable Neodymium permanent magnet (dimension: $60 \times 30 \times 15$ mm^3) provides an external magnetic field of $\mu_0 H_{ext} = 390$ mT at the probed sample region under an angle ξ with respect to the surface normal.

UXRD measurement

In the UXRD experiment, the heterostructures are excited by a 60 fs pump-pulse with a central wavelength of 800 nm incident at 50° with respect to the sample normal with a repetition rate of 1 kHz and a beam footprint of 750×840 μm^2. The incident angle α_{in} of the 200 fs-long hard X-ray probe pulses with a photon energy of ≈ 8 keV provided by a table-top laser-based plasma X-ray source[53] is kept fixed at 19.5° to probe the strain response of the Pt layer and at 22.1° for the Cu and Ni layers. At an intermediate angle, we are able to record all three Bragg peaks simultaneously[42] on a pixelated area detector as displayed in the detector inset of Fig. 3a that sketches the experimental geometry with the pump beam incident at 50° with respect to the sample normal.

Modeling strain response

To model the strain response, we use the modular PYTHON library UDKM1DSIM[54] and a single set of thermo-physical parameters stated in Table 1. In the first step, we calculate the absorption profile utilizing a transfer matrix approach[57] utilizing literature values for the refractive index $\tilde{n}$ at 800 nm given in Table 1. Starting from the calculated depth-dependent energy deposition, we solve the diffusive two-temperature model[42,43] to determine the spatiotemporal distribution of the laser-deposited energy within the heterostructures, which linearly relates to a spatiotemporal laser-

induced stress via subsystem-specific Grüneisen parameters Γ_r[42]. The solution of the elastic wave equation for these stress contributions yields the spatio-temporal strain response, which is translated into Bragg peak shifts via dynamical X-ray diffraction theory that yields the transient layer-specific strain as in the UXRD experiment. Details of our model approach were reported previously[42].

Data availability

The datasets generated during and/or analyzed during the current study are available from the corresponding author upon reasonable request.

References

1. Beaurepaire, E., Merle, J.-C., Daunois, A. & Bigot, J.-Y. Ultrafast spin dynamics in ferromagnetic nickel. *Phys. Rev. Lett.* **76**, 4250 (1996).
2. Hohlfeld, J., Matthias, E., Knorren, R. & Bennemann, K. Nonequilibrium magnetization dynamics of nickel. *Phys. Rev. Lett.* **78**, 4861 (1997).
3. Stamm, C., Pontius, N., Kachel, T., Wietstruk, M. & Dürr, H. Femtosecond x-ray absorption spectroscopy of spin and orbital angular momentum in photoexcited Ni films during ultrafast demagnetization. *Phys. Rev. B* **81**, 104425 (2010).
4. Koopmans, B. et al. Explaining the paradoxical diversity of ultrafast laser-induced demagnetization. *Nat. Mater.* **9**, 259–265 (2010).
5. You, W. et al. Revealing the nature of the ultrafast magnetic phase transition in ni by correlating extreme ultraviolet magneto-optic and photoemission spectroscopies. *Phys. Rev. Lett.* **121**, 077204 (2018).
6. Ma, T. et al. Distinguishing the laser-induced spin precession excitation mechanism in Fe/MgO (001) through field orientation dependent measurements. *J. Appl. Phys.* **117**, 013903 (2015).
7. Bigot, J.-Y., Vomir, M., Andrade, L. & Beaurepaire, E. Ultrafast magnetization dynamics in ferromagnetic cobalt: The role of the anisotropy. *Chem. Phys.* **318**, 137–146 (2005).
8. Van Kampen, M., Koopmans, B., Kohlhepp, J. & De Jonge, W. Laser-induced precession in canted-spin ferromagnets. *J. Magn. Magn. Mater.* **240**, 291–293 (2002).
9. Kats, V. et al. Ultrafast changes of magnetic anisotropy driven by laser-generated coherent and noncoherent phonons in metallic films. *Phys. Rev. B* **93**, 214422 (2016).
10. Van Kampen, M. et al. All-optical probe of coherent spin waves. *Phys. Rev. Lett.* **88**, 227201 (2002).
11. Shin, Y. et al. Quasi-static strain governing ultrafast spin dynamics. *Commun. Phys.* **5**, 56 (2022).
12. Shin, Y., Yoon, S., Hong, J.-I. & Kim, J.-W. Magnetoelasticity-driven phase inversion of ultrafast spin precession in Ni_xFe_{100-x} thin films. *J. Sci.* **8**, 100568 (2023).
13. Scherbakov, A. et al. Coherent magnetization precession in ferromagnetic (Ga, Mn)As induced by picosecond acoustic pulses. *Phys. Rev. Lett.* **105**, 117204 (2010).
14. Kim, J.-W., Vomir, M. & Bigot, J.-Y. Ultrafast magnetoacoustics in nickel films. *Phys. Rev. Lett.* **109**, 166601 (2012).
15. Jäger, J. et al. Picosecond inverse magnetostriction in galfenol thin films. *Appl. Phys. Lett.* **103**, 032409 (2013).
16. Bombeck, M. et al. Magnetization precession induced by quasitransverse picosecond strain pulses in (311) ferromagnetic (ga, mn) as. *Phys. Rev. B* **87**, 060302 (2013).
17. Kim, J.-W., Vomir, M. & Bigot, J.-Y. Controlling the spins angular momentum in ferromagnets with sequences of picosecond acoustic pulses. *Sci. Rep.* **5**, 8511 (2015).
18. Kim, J.-W. & Bigot, J.-Y. Magnetization precession induced by picosecond acoustic pulses in a freestanding film acting as an acoustic cavity. *Phys. Rev. B* **95**, 144422 (2017).
19. Razdolski, I. et al. Nanoscale interface confinement of ultrafast spin transfer torque driving non-uniform spin dynamics. *Nat. Commun.* **8**, 15007 (2017).
20. Igarashi, J. et al. Optically induced ultrafast magnetization switching in ferromagnetic spin valves. *Nat. Mater.* **22**, 725–730 (2023).
21. Rongione, E. et al. Emission of coherent THz magnons in an antiferromagnetic insulator triggered by ultrafast spin–phonon interactions. *Nat. Commun.* **14**, 1818 (2023).
22. Alebrand, S. et al. Light-induced magnetization reversal of high-anisotropy TbCo alloy films. *Appl. Phys. Lett.* **101**, 162408 (2012).
23. Mangin, S. et al. Engineered materials for all-optical helicity-dependent magnetic switching. *Nat. Mater.* **13**, 286–292 (2014).
24. Stanciu, C. D. et al. All-optical magnetic recording with circularly polarized light. *Phys. Rev. Lett.* **99**, 047601 (2007).
25. Kovalenko, O., Pezeril, T. & Temnov, V. V. New concept for magnetization switching by ultrafast acoustic pulses. *Phys. Rev. Lett.* **110**, 266602 (2013).
26. Bandyopadhyay, S., Atulasimha, J. & Barman, A. Magnetic straintronics: manipulating the magnetization of magnetostrictive nanomagnets with strain for energy-efficient applications. *Appl. Phys. Rev.* **8**, 041323 (2021).
27. Yang, W.-G. & Schmidt, H. Acoustic control of magnetism toward energy-efficient applications. *Appl. Phys. Rev.* **8**, 021304 (2021).
28. Dolgikh, A. et al. Ultrafast heat-assisted magnetization dynamics in a ferrimagnetic insulator. *Phys. Rev. B* **107**, 094424 (2023).
29. Vernik, U. et al. Resonant phonon-magnon interactions in freestanding metal-ferromagnet multilayer structures. *Phys. Rev. B* **106**, 144420 (2022).
30. Bojahr, A. et al. Second harmonic generation of nanoscale phonon wave packets. *Phys. Rev. Lett.* **115**, 195502 (2015).
31. Lee, S. H. et al. Generation and propagation of a picosecond acoustic pulse at a buried interface: time-resolved x-ray diffraction measurements. *Phys. Rev. Lett.* **95**, 246104 (2005).
32. Zeuschner, S. P. et al. Tracking picosecond strain pulses in heterostructures that exhibit giant magnetostriction. *Struct. Dyn.* **6**, 024302 (2019).
33. Trigo, M. et al. Probing unfolded acoustic phonons with X rays. *Phys. Rev. Lett.* **101**, 025505 (2008).
34. Jäger, J. et al. Resonant driving of magnetization precession in a ferromagnetic layer by coherent monochromatic phonons. *Phys. Rev. B* **92**, 020404 (2015).
35. Mattern, M., Pudell, J.-E., Laskin, G., von Reppert, A. & Bargheer, M. Analysis of the temperature-and fluence-dependent magnetic stress in laser-excited $SrRuO_3$. *Struct. Dyn.* **8**, 024302 (2021).
36. von Reppert, A. et al. Spin stress contribution to the lattice dynamics of FePt. *Sci. Adv.* **6**, eaba1142 (2020).
37. Pudell, J. et al. Ultrafast negative thermal expansion driven by spin disorder. *Phys. Rev. B* **99**, 094304 (2019).
38. Mattern, M., Pudell, J.-E., Dumesnil, K., von Reppert, A. & Bargheer, M. Towards shaping picosecond strain pulses via magnetostrictive transducers. *Photoacoustics* **30**, 100463 (2023).
39. Pudell, J. et al. Layer specific observation of slow thermal equilibration in ultrathin metallic nanostructures by femtosecond x-ray diffraction. *Nat. Commun.* **9**, 3335 (2018).
40. Herzog, M. et al. Phonon-dominated energy transport in purely metallic heterostructures. *Adv. Funct. Mater.* **32**, 2206179 (2022).
41. Mattern, M. et al. Electronic energy transport in nanoscale Au/Fe hetero-structures in the perspective of ultrafast lattice dynamics. *Appl. Phys. Lett.* **120**, 092401 (2022).
42. Mattern, M. et al. Concepts and use cases for picosecond ultrasonics with X-rays. *Photoacoustics* **31**, 100503 (2023).

43. Pudell, J.-E. et al. Heat transport without heating?—an ultrafast x-ray perspective into a metal heterostructure. *Adv. Funct. Mater.* **30**, 2004555 (2020).

44. Ferté, T. et al. Ultrafast hot-electron induced quenching of tb 4 f magnetic order. *Phys. Rev. B* **96**, 144427 (2017).

45. Ferté, T. et al. Ultrafast demagnetization in buried co80dy20 as fingerprint of hot-electron transport. *J. Magn. Magn. Mater.* **485**, 320–324 (2019).

46. Deb, M. et al. Picosecond acoustic-excitation-driven ultrafast magnetization dynamics in dielectric bi-substituted yttrium iron garnet. *Phys. Rev. B* **98**, 174407 (2018).

47. Deb, M. et al. Generation of spin waves via spin-phonon interaction in a buried dielectric thin film. *Phys. Rev. B* **103**, 024411 (2021).

48. Zeuschner, S. P. et al. Standing spin wave excitation in Bi:YIG films via temperature-induced anisotropy changes and magneto-elastic coupling. *Phys. Rev. B* **106**, 134401 (2022).

49. Xu, Y. et al. Ultrafast magnetization manipulation using single femtosecond light and hot-electron pulses. *Adv. Mater.* **29**, 1703474 (2017).

50. Bergeard, N. et al. Hot-electron-induced ultrafast demagnetization in co/pt multilayers. *Phys. Rev. Lett.* **117**, 147203 (2016).

51. Bergeard, N. et al. Tailoring femtosecond hot-electron pulses for ultrafast spin manipulation. *Appl. Phys. Lett.* **117**, 222408 (2020).

52. Zeuschner, S. et al. Reciprocal space slicing: a time-efficient approach to femtosecond x-ray diffraction. *Struct. Dyn.* **8**, 014302 (2021).

53. Schick, D. et al. Normalization schemes for ultrafast X-ray diffraction using a table-top laser-driven plasma source. *Rev. Sci. Instrum.* **83**, 025104 (2012).

54. Schick, D. udkm1dsim—a python toolbox for simulating 1d ultrafast dynamics in condensed matter. *Comput. Phys. Commun.* **266**, 108031 (2021).

55. MacFarlane, R., Rayne, J. & Jones, C. Temperature dependence of elastic moduli of iridium. *Phys. Lett.* **20**, 234–235 (1966).

56. Mattern, M., Weber, F.-C., Engel, D., von Korff Schmising, C. & Bargheer, M. Coherent control of magnetization precession by double-pulse activation of effective fields from magnetoacoustics and demagnetization. *Appl. Phys. Lett.* **124**, 102402 (2024).

57. Khorsand, A., Savoini, M., Kirilyuk, A. & Rasing, T. Optical excitation of thin magnetic layers in multilayer structures. *Nat. Mater.* **13**, 101–102 (2014).

58. Werner, W. S., Glantschnig, K. & Ambrosch-Draxl, C. Optical constants and inelastic electron-scattering data for 17 elemental metals. *J. Phys. Chem. Ref. Data* **38**, 1013–1092 (2009).

59. Stephens, R. E. & Malitson, I. H. Index of refraction of magnesium oxide. *J. Res. Natl. Bur. Stand.* **49**, 249–252 (1952).

60. Corning Incorporated. *Corning 1737 AMLCD Glass* (2002).

61. Hohlfeld, J. et al. Electron and lattice dynamics following optical excitation of metals. *Chem. Phys.* **251**, 237–258 (2000).

62. Lin, Z., Zhigilei, L. V. & Celli, V. Electron-phonon coupling and electron heat capacity of metals under conditions of strong electron-phonon nonequilibrium. *Phys. Rev. B* **77**, 075133 (2008).

63. Bodryakov, V. Y. & Bashkatov, A. Heat capacity of tantalum in the normal and superconducting states: Identification of the contributions. *Russian Metall.* **2013**, 671–675 (2013).

64. Shayduk, R. et al. Nanosecond laser pulse heating of a platinum surface studied by pump-probe X-ray diffraction. *Appl. Phys. Lett.* **109**, 043107 (2016).

65. Meschter, P. J., Wright, J. W., Brooks, C. R. & Kollie, T. G. Physical contributions to the heat capacity of nickel. *J. Phys. Chem. Solids* **42**, 861–871 (1981).

66. Barron, T., Berg, W. & Morrison, J. On the heat capacity of crystalline magnesium oxide. *Proc. R. Soc. Lond. Ser. A Math. Phys. Sci.* **250**, 70–83 (1959).

67. Duggin, M. The thermal conductivities of aluminium and platinum. *J. Phys. D* **3**, L21 (1970).

68. Slifka, A. J., Filla, B. J. & Phelps, J. Thermal conductivity of magnesium oxide from absolute, steady-state measurements. *J. Res. Natl. Inst. Stand. Technol.* **103**, 357 (1998).

69. Zahn, D., Seiler, H., Windsor, Y. W. & Ernstorfer, R. Ultrafast lattice dynamics and electron–phonon coupling in platinum extracted with a global fitting approach for time-resolved polycrystalline diffraction data. *Struct. Dyn.* **8**, 064301 (2021).

70. Overton Jr, W. & Gaffney, J. Temperature variation of the elastic constants of cubic elements. I. copper. *Phys. Rev.* **98**, 969 (1955).

71. Neighbours, J., Bratten, F. & Smith, C. S. The elastic constants of nickel. *J. Appl. Phys.* **23**, 389–393 (1952).

72. Featherston, F. H. & Neighbours, J. Elastic constants of tantalum, tungsten, and molybdenum. *Phys. Rev.* **130**, 1324 (1963).

73. Durand, M. A. The temperature variation of the elastic moduli of NaCl, KCl and MgO. *Phys. Rev.* **50**, 449 (1936).

74. Krishnan, R., Srinivasan, R. & Devanarayanan, S. Chapter 5—thermal expansion data. In *Thermal Expansion of Crystals*, vol. 12 of *International Series in the Science of the Solid State*, 115–194 (Pergamon, 1979).

75. Wang, X. et al. Electronic Grüneisen parameter and thermal expansion in ferromagnetic transition metal. *Appl. Phys. Lett.* **92**, 121918 (2008).

76. Nix, F. & MacNair, D. The thermal expansion of pure metals. ii: molybdenum, palladium, silver, tantalum, tungsten, platinum, and lead. *Phys. Rev.* **61**, 74 (1942).

77. Nix, F. & MacNair, D. The thermal expansion of pure metals: copper, gold, aluminum, nickel, and iron. *Phys. Rev.* **60**, 597 (1941).

78. White, G. & Anderson, O. Grüneisen parameter of magnesium oxide. *J. Appl. Phys.* **37**, 430–432 (1966).

Acknowledgements

Author contributions

J.J. conducted and analyzed MOKE experiments. Static magnetic characterization was done by J.-C.R.S. and F.-C.W. M.M., J.-E.P., and A.vR. conducted the UXRD experiments and modeled the UXRD data together with J.J. The MOKE modeling was done by J.J. and F.-C.W., with important contributions from X.-G.W. The heterostructure series was prepared by M.H. A.vR. proposed the study and supervised it together with M.B. The paper was written by M.M., J.J., and M.B. using the Figures created by J.J.

Funding

Competing interests

The authors declare no competing interests.

Additional information

Correspondence and requests for materials should be addressed to Maximilian Mattern or Matias Bargheer.

Peer review information *Communications Physics* thanks Hiroki Wadati, Antonio Caretta and the other, anonymous, reviewer(s) for their contribution to the peer review of this work.

Reprints and permissions information is available at http://www.nature.com/reprints